Journal of Applied Geophysics 208 (2023) 104889

Contents lists available at ScienceDirect

Journal of Applied Geophysics

journal homepage: www.elsevier.com/locate/jappgeo

Detecting hypogenic karst features in the northeastern Delaware Basin, west Texas: Applications of Full Tensor Gradient (FTG) gravity data

Hualing Zhang [a,b,*], Dale E. Bird [b,c]

[a] Research Institute of Petroleum Exploration & Development, PetroChina, Beijing 100083, China
[b] Department of Earth and Atmospheric Sciences, University of Houston, Houston, TX 77204-5007, USA
[c] Bird Geophysical, Houston, TX 77084, USA

ARTICLE INFO

Keywords:
Airborne gravity gradiometry data
3D gravity inversion
Hypogenic karst
Delaware Basin

ABSTRACT

Extensive karst development in carbonate and evaporate strata often occur in the Upper Permian formations of the Delaware Basin, west Texas. Subsurface karst feature detection is essential since they may cause severe drilling geohazards. In order to detect subsurface karst features, we present an interpretation approach that integrates high-resolution, high-precision airborne full tensor gradiometry (FTG) gravity data, structural interpretations, density and lithological variations derived from well logs, and published seismic refraction data, with regional cross sections to produce a geologically plausible 3D FTG model in the northeastern Delaware Basin. Both traditional gravity (Tz) and FTG (Tzz) density inversions were carried out on three shallow sedimentary layers of the Ochoan-lower Permian section, demonstrating the subtle density distribution in these strata. Detailed low-density karst boundaries were then interpretated by making use of the intrinsic properties of the gradient components, Txz and Tyz, which are: 1) edge detectors, because anomaly maxima and minima are located directly over source boundaries, and 2) indicators of the direction of density change across these boundaries. Source boundaries, or faults, mapped from these components were integrated and combined with regional geology and measured densities to verify existing faults, infer new faults, and predict probable locations and shapes of karst cavities in the southwestern and northeastern parts of the study area. Our results show that the central and southwestern parts of the study area may represent higher drilling risks due to an increase in shallow karst geohazards. This interpretation approach may be used to detect fault systems and geometries of low-density or high-density source geobodies worldwide.

1. Introduction

The Permian Basin of West Texas and southeast New Mexico is located in the foreland area of the Ouachita-Marathon fold-thrust belt, and it is divided into three major structural components: the Delaware and Midland Basins are separated by the Central Basin Platform on the west and east, respectively (Fig. 1a, b). Extensive karst development in carbonate and evaporate strata occur in shallow sediments of the Delaware Basin and are mainly associated with late Permian Guadalupian and Ochoan strata (Stafford, 2017; Fig. 1c). Recent studies of hypogenic karst features have focused on outcrops (Castile and Rustler formations) within the western and central Delaware Basin (e.g., Scholle et al., 2004; Stafford, 2013; Stafford, 2017; Majzoub et al., 2017; Stafford et al., 2018). In the Castile formation, a range of hypogene speleogenesis commonly occur, from deep isolated rise structures (~100 m) to cave mazes and intra-stratal brecciation (Stafford, 2017; Fig. 1d). Hypogene karst in shallow Salado and Rustler formations are largely associated with cross-formational breccia pipes and intra-stratal brecciation (Stafford, 2017; Fig. 1d). However, in the eastern portion of the Delaware Basin, much of the soluble rock is buried beneath northeast dipping strata (Fig. 1d), as a result, these regions are less studied.

New approaches are required to improve our understanding of subsurface hypogene karst features, because they are often linked to costly geohazards during drilling operations. When wells penetrate subsurface karst features, a spectrum of problems may occur, from increased wellbore washout, to total loss of drilling fluid, to abandonment of the surface hole location (Hoang et al., 2019). In addition to these problems, large karsts may cause bit drops, and even pose drilling risks and damage to production surface equipment (Hoang et al., 2019). For example, in their conference poster, Morgan et al. (2018) reported that a drilling

* Corresponding author at: Research Institute of Petroleum Exploration & Development, PetroChina, Beijing 100083, China.
E-mail address: hzhang67@uh.edu (H. Zhang).

https://doi.org/10.1016/j.jappgeo.2022.104889
Received 16 June 2021; Received in revised form 24 October 2022; Accepted 22 November 2022
Available online 24 November 2022

operator in Culbertson County, western Delaware Basin, experienced significant drilling fluid loss in several wells after penetrating open voids within the initial 500 ft., forcing them to abandon the boreholes. The Permian Basin is the most prolific oil-producing basin in the United States (Dutton et al., 2004, 2005); therefore, subsurface karst detection is necessary to avoid drilling geohazards.

High-resolution, high-precision FTG data is an exploration tool used to detect and map source bodies defined by subtle density contrasts, especially those within close proximity to the measurement platform. Its short wavelength resolution enables the identification of small density sources required for detailed hydrocarbon and mineral exploration. Varied and successful applications using the Tzz component include salt dome detection in Louisiana, USA (Murphy and Mumaw, 2004), low-density sedimentary deposits mapped in the Judd Basin, offshore NW Europe (Murphy and Mumaw, 2004), and the detection of intrusion-hosted sulphide mineralization in Newfoundland, Canada (Mataragio and Kieley, 2009). Our application of FTG data for karst detection is consistent with these examples because shallow karst voids are typically less dense than their host rocks. Examples in the Permian Basin include analyses by Hoang et al. (2019) and Sallee et al. (2019). However, these studies focused on analyses of Tzz components, with only cursory references to the other five gravity tensors.

Our study of dissolution karsting makes use of Txz, Tyz and Tzz FTG components to infer caverns, systems of caverns, and zones with high porosity in the northeastern Delaware Basin (Fig. 1a). We employed two approaches: 1) a typical 3D model with density inversions from gravity and gravity gradient (Tzz only) data, and 2) an examination of Txz and Tyz gradient components, extending Veryaskin and McRae (2008) hypothetical model results to our study area by mapping possible karst source body edges and associated low-density regions in the Delaware Basin. Our results demonstrate how these data may help de-risk related geohazards, and our interpretation method may be applied to similar regions around the world.

2. Dataset and method

The airborne, terrain-corrected FTG gravity survey was flown by Bell Geospace, covering about 144 km^2, over intersecting parts of Loving, Ward, and Reeves Counties (Fig. 2a), with survey lines spaced every 50 m (Fig. 2b). The FTG survey was terrain-corrected using Bell Geospace's accurate digital terrain model, and the terrain relief within the survey area is <80 m. The data was then leveled and denoised by Bell Geospace. A NW-SE trending normal fault mapped by Ruppel et al. (2008) cuts into the survey area, which we refer to as the Loving Fault, that is possibly bounded a its southern extent by the *E*-W trending Grisham strike-slip fault (Fig. 2a). Nine well logs provided by Enverus were projected into

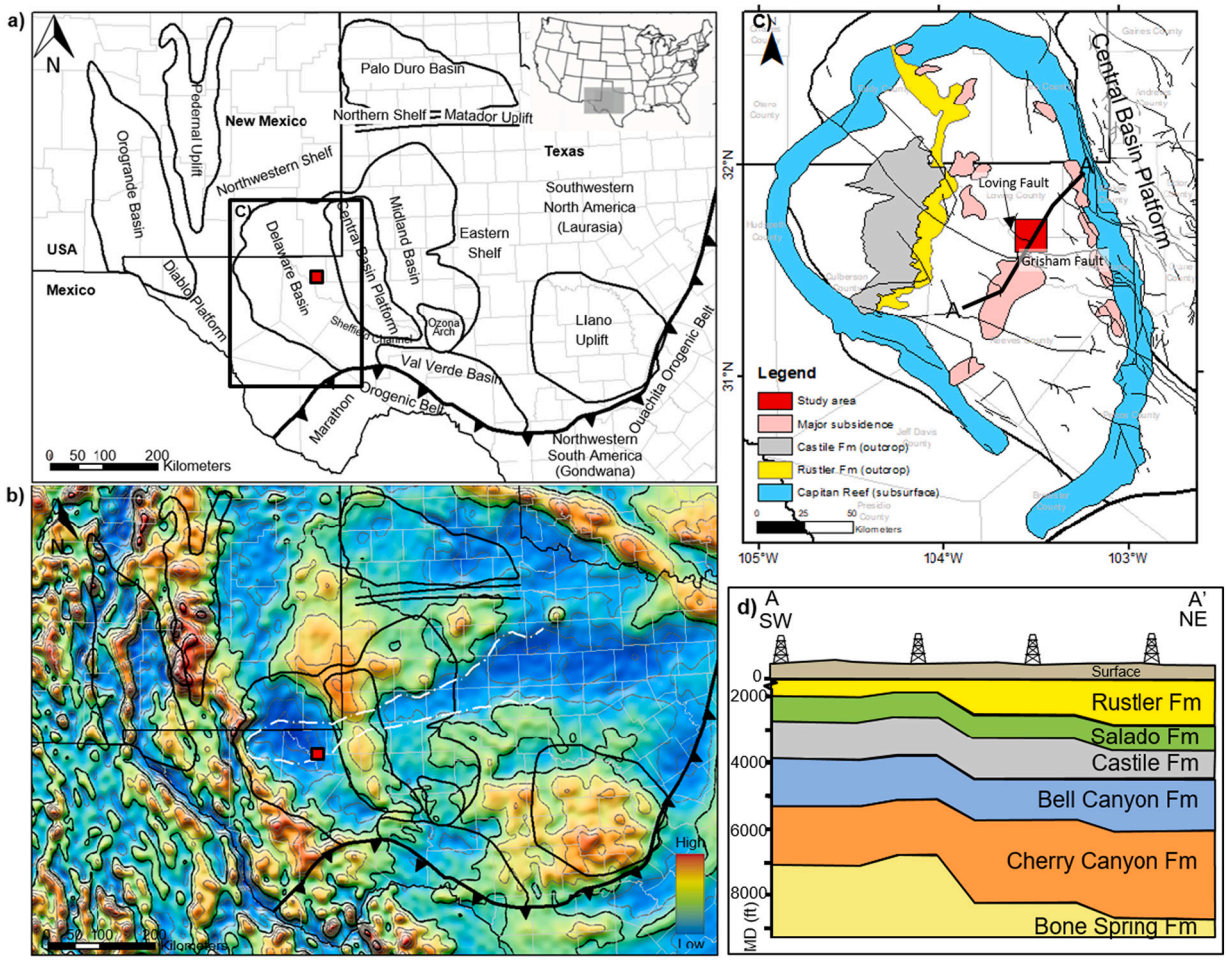

Fig. 1. a) Physiographic setting of the Permian Basin with major basin names and the study area outlined by the red box (modified from Zhang et al., 2021). (b) Regional Bouguer gravity anomalies over the Permian Basin show major basins and regional structures, such as the Central Basin Platform (modified from Garcia et al., 2014). c) Geological map of the Delaware Basin with the locations of selected major units related to hypogenic karst features. Paleozoic fault distribution (thin black lines) was mapped by Ruppel et al. (2008) and Ewing et al. (2019), including the Grisham Fault and the Loving Fault. d) Cross-section (flattened on the top Rustler layer) through the study area, based on well correlations, depicting stratigraphic units in the northeastern Delaware Basin with a northeast dip. (For interpretation of the references to colour in this figure legend, the reader is referred to the web version of this article.)

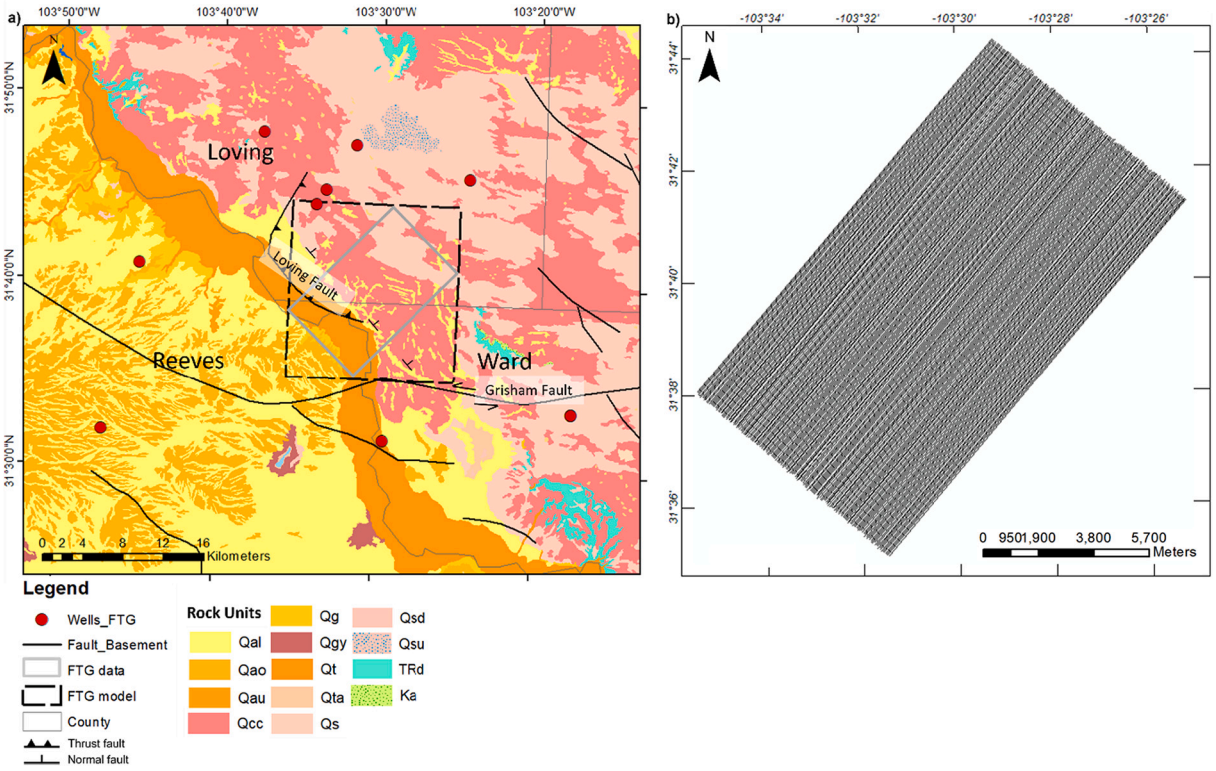

Fig. 2. a) Geologic map of the study area and FTG survey area (grey box). The 3D model area is outlined by the black dashed line. Well locations of logs used in the study are shown as red dots. Faults are represented by black lines, including the strike-slip Grisham and the reverse Loving Faults. Fault locations were mapped by Ruppel et al. (2008). b) Flight lines of the FTG survey spaced every 50 m. (For interpretation of the references to colour in this figure legend, the reader is referred to the web version of this article.)

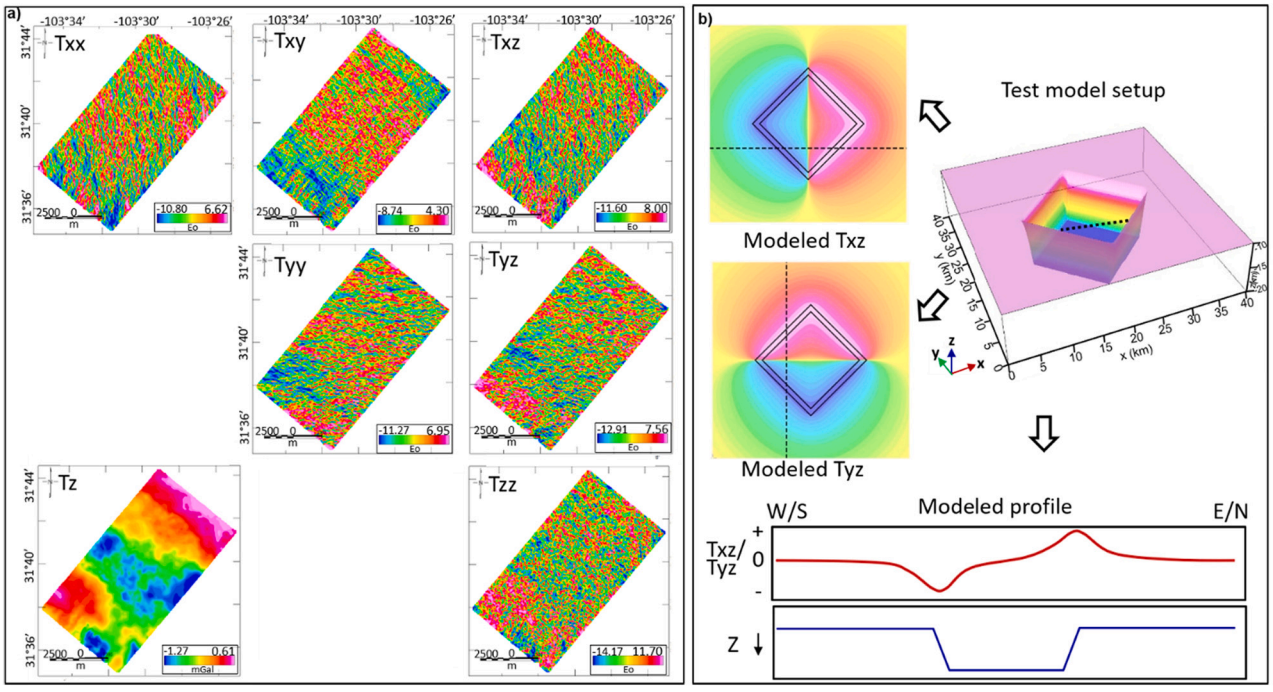

Fig. 3. a) FTG survey data showing the six gravity tensors and gravity (Tz). b) Test model shows the response of Txz and Tyz component anomalies over a low-density prism. Plan-view dashed lines are identical, relative to x and y directions, and therefore may be represented by a single cross-section below. Note that anomalies along these lines overlie the same structural trends, following the NED calculation standard. That is, Txz is calculated from west to east, and Tyz is calculated from south to north.

the survey area for stratigraphic, lithological, and density control (Fig. 2a).

Gravity gradients are measures of the spatial rate of change of gravitational acceleration. Gravitational acceleration $\vec{g}$ is the gradient of gravitational potential, Φ, as shown below (Martinez et al., 2013),

$$\vec{g} = \nabla\Phi = \left(\frac{\partial\Phi}{\partial x}, \frac{\partial\Phi}{\partial x}, \frac{\partial\Phi}{\partial x}\right) = (g_x, g_y, g_z). \quad (1)$$

The gradient of the acceleration, $\vec{g}$, is the gravity gradient tensor field, T (Telford et al., 1990), defined as,

$$\mathrm{T} = \nabla\vec{g} = \nabla\nabla\Phi = \begin{bmatrix} \frac{\partial^2\Phi}{\partial x^2} & \frac{\partial^2\Phi}{\partial x\partial y} & \frac{\partial^2\Phi}{\partial x\partial z} \\ \frac{\partial^2\Phi}{\partial y\partial x} & \frac{\partial^2\Phi}{\partial y^2} & \frac{\partial^2\Phi}{\partial y\partial z} \\ \frac{\partial^2\Phi}{\partial z\partial x} & \frac{\partial^2\Phi}{\partial z\partial y} & \frac{\partial^2\Phi}{\partial z^2} \end{bmatrix} = \begin{bmatrix} T_{xx} & T_{xy} & T_{xz} \\ T_{yx} & T_{yy} & T_{yz} \\ T_{zx} & T_{zy} & T_{zz} \end{bmatrix}. \quad (2)$$

The earth's gravity field is a smooth vector field; it is conservative, harmonic, irrotational, solenoidal, it satisfies Laplace's equation in source-free regions, and its gradient tensor is symmetric and traceless (Blakely, 1995): i.e., Txy = Tyx, Txz = Tzx, and Tyz = Tzy (symmetry), and the Laplacian, Txx + Tyy + Tzz = 0 (zero trace). Reconciling gravity (Tz) and gravity gradient (Tzz) amplitude units reveal an enormous difference in resolution. Consider gradient units (Eotvos, or Eo) in terms of gravity units (mGal/m): 100 Eo = 1/100 mGal/m. This means that gradient data can resolve anomalies produced by far smaller density variations than conventional gravity data can resolve.

Five independent tensor components together with the vertical tensor component and gravity (Tz) are displayed in Fig. 3a. Based on the survey size, line spacing and measured wavelengths between 170 and 16,000 m, the FTG data used in this study has far greater resolution than the regional open-file gravity data (Murphy, 2004; Dransfield et al., 2010). Each tensor component represents directional changes in the magnitude of the tensor field, and they can therefore be associated with different attributes of geology (Bell et al., 1997; Murphy and Mumaw, 2004; Stasinowsky, 2010). For example, source edges or lateral changes in density such as faults produce Txz and Tyz anomaly maxima/minima directly over these density contrasts (Bell et al., 1997; Murphy and Dickson, 2009; Ennen, 2012). Tzz anomaly maxima and minima are located over centers of respective high and low density areas (Bell et al., 1997; Ennen, 2012). Gravity gradient data are processed to follow the North-East-Down (NED) standard (Bell et al., 1997) as shown by the test model in Fig. 3b. That is, Txz is calculated from west to east, and Tyz is calculated from south to north. The test model shows FTG anomalies over a low-density prism that simulates a karst feature. Note that Txz anomalies are produced by density contrasts that trend roughly N-S, and Tyz anomalies are produced by density contrasts that trend roughly *E*-W. The profile below the test model in Fig. 3b shows the changes of Txz and Tyz anomalies moving from west to east and south to north. Peaks are produced over the edges of the low-density prism in the test model.

A 3D FTG model was created, using Seequent's *Oasis Montaj* software, which employs forward and inverse frequency-domain algorithms (Cordell and Henderson, 1968; Parker, 1973; Bott, 2012; Li and Chouteau, 1998). The model map view and vertical cell dimensions were 50 m and 10 m, respectively (334,348 total cells). Calculations were performed in the wave number domain based on Dr. Bill Pearson's implementation of R. L. Parker's algorithm (1972). The model included ten layers: seven sedimentary, two crystalline crust, and an upper mantle (Fig. 4b). The seven sedimentary layers included: 1) topography - top Rustler Formation, 2) top Rustler - top Leonardian Formation, 3) top Leonardian - top Strawn Formation, 4) top Strawn - top Barnett Formation, 5) top Barnett - top Devonian (Woodford Formation), 6) top Barnett - top Ellenburger Formation, and 7) top Ellenburger Formation to top basement. The model was built from structural and density grids extracted from a recent basin-scale model (Zhang et al., 2021; Fig. 4a). In the basin-scale model, the formation tops of each sedimentary layer were correlated from 296 well logs throughout the Permian Basin and then gridded to 4 km cells (Zhang et al., 2021). Average density values within each layer were calculated at each well location (1614 measurements) and then gridded to 4 km cells (Zhang et al., 2021). The densities of upper crust, lower crust, and upper mantle used in the regional model were 2.75, 2.9, 3.3 g/cc, respectively (Zhang et al., 2021). These density values are consistent with ranges of densities applied to crust and mantle layers in previous studies (i.e., Adams and Keller, 1996; Hall et al., 2018). The structural and density grids used in this study were extracted from the regional model grids and then re-gridded for the model in this study to a 50 m cells.

A structural inversion of the Moho horizon was first conducted to improve the long-wavelength crustal geometry in the study area. Then,

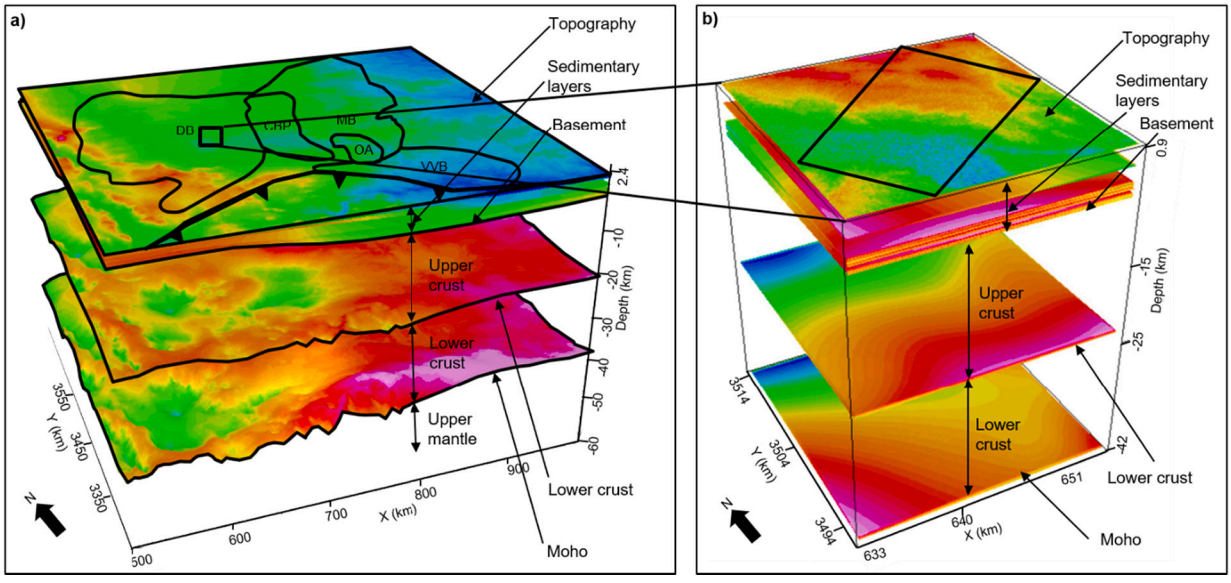

Fig. 4. 3D gravity model setup. a) Regional 3D gravity model in the Permian Basin generated by Zhang et al. (2021). Abbreviations: DB: Delaware Basin; CBP: Central Basin Platform; MB: Midland Basin; OA: Ozona Arch; VVB: Val Verde Basin. b) 3D FTG model based on structural and density grids extracted from the regional 3D model shown in a). The location of the FTG survey area is shown in the black SW-NE-oriented rectangle.

density inversions of gravity (Tz) anomalies were calculated for the top two sedimentary layers individually (topography-top Rustler and top Rustler-top Leonardian), and for these combined layers (topography- top Leonardian). Below we refer to these respective layers as Surface, Rustler, and Combined. Convergence limits for Tz and Tzz density inversions were 1 mGal and 10 Eo, respectively. Tz density inversions converged after 169, 122, and 126 iterations for the Surface, Rustler, and Combined layer, respectively. After achieving a satisfactory Tz inversion result (RMS difference between calculated and measured data <0.8 mGal), we conducted density inversions using the Tzz gradient component to capture more subtle density variations in the sedimentary layers. We set final layer densities from the Tz inversions equal to the initial densities for the gradient (Tzz) inversions and followed the same workflow as above.: Tzz inversions converged after 257, 106, and 72 iterations for Surface, Rustler, and Combined layer, respectively.

3. Results

In order to make quantitative comparisons of inversion results between Surface, Rustler, and Combined sedimentary layers for all density inversions (Figs. 5-8), we first normalized the colour stretch such that colors have equivalent values for all three difference grids (Figs. 5-8, a-c). We then plotted the number of difference values as a function of the actual difference (Eo), thus allowing direct comparisons of the difference results between the inversions (Figs. 5-8, d). These plots are a measure of inversion accuracy; that is, difference ranges, and how often they occur over the study area, are directly compared for all gradient components.

3.1. Density inversion of gravity (Tz) anomalies

Fig. 5 shows Tz density inversion results of the Surface, Rustler, and Combined sedimentary layers. Density inversion of the surface layer converged after 169 iterations. The Tz inversion result is fair, even though the difference range (between observed and calculated gravity) was small (−0.30 to 0.61mGal). Fig. 5d shows the distribution of the normalized difference between the observed and calculated gravity (blue line). Relatively few well logs were available to examine in the Surface layer (<80), while more well logs were available for deeper layers (>200). Therefore, the normalized difference of the Surface layer is less constrained (Fig. 5a), which is reflected in the broader range of values compared to the other inversion results (Fig. 5d).

The density inversion of the Rustler layer converged after 122 iterations and resolved gravity high trends over the northeastern part of study area and near the Loving fault (Fig. 5b). The fit between calculated and observed gravity anomalies is better than the Surface layer, with a difference range of −0.06 to 0.21mGal (Fig. 5b). The normalized difference has a narrower range, as shown in Fig. 5b and Fig. 5d. The gravity maximum over the southwest part of the study area is interpreted to be produced by the previously mapped Loving Fault (Fig. 2; Fig. 5b; Ruppel et al., 2008). The Loving Fault is shown as a gravity high and thought to be produced by lateral changes in density along the edge of the fault. We suggest that another high amplitude gravity anomaly along the northeast boundary of the study area may be produced by an

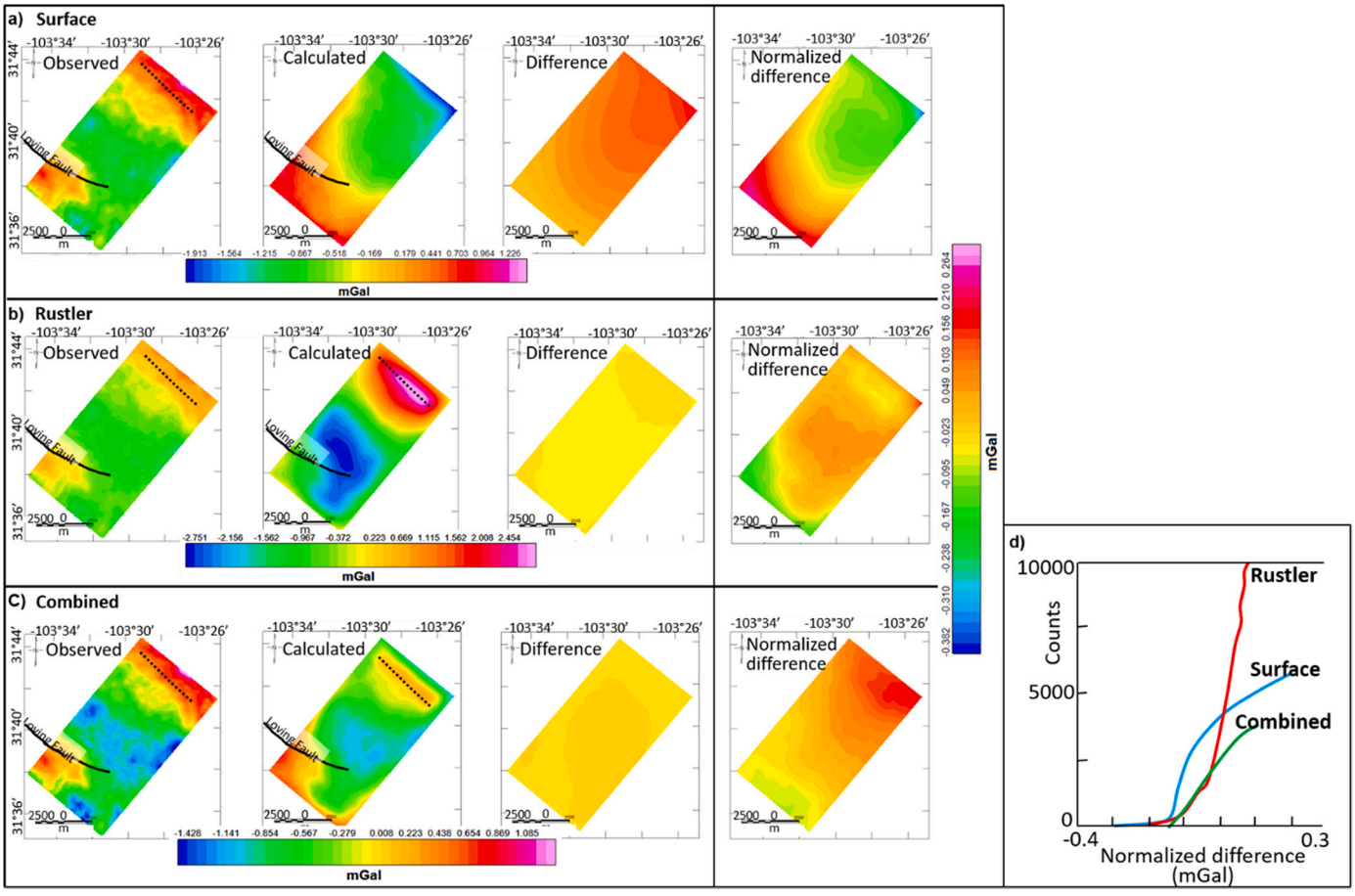

Fig. 5. Density inversion results of Tz gravity, showing observed, calculated, difference, and normalized difference anomalies: a) Surface layer,. b) Rustler layer. c) Combined layer. The location of the Loving Fault is shown in the black line (modified from Ruppel et al., 2008). The dotted line shows the location of a possible unmapped fault. d) Normalized difference anomaly distributions between the observed and calculated gravity of the Surface, Rustler, and Combined layers (see text for explanation).

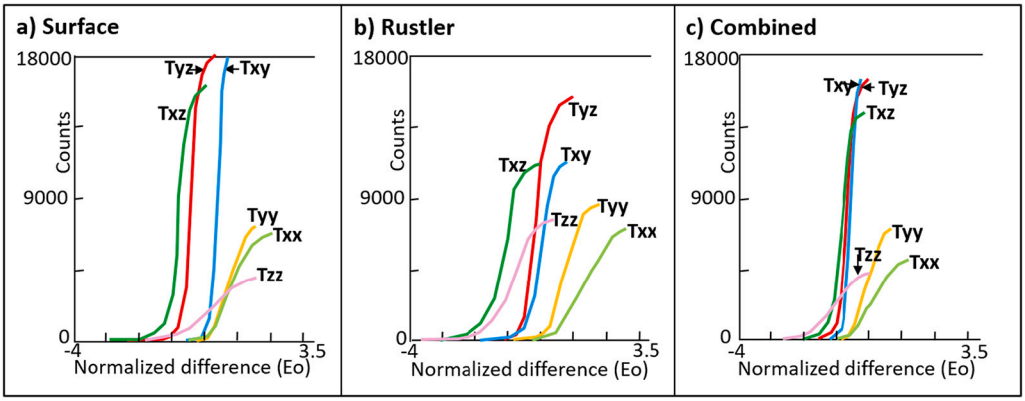

Fig. 6. Normalized difference distributions of all six gravity gradient components, after Tzz density inversion: a) Surface layer. b) Rustler layer. c) Combined layer.

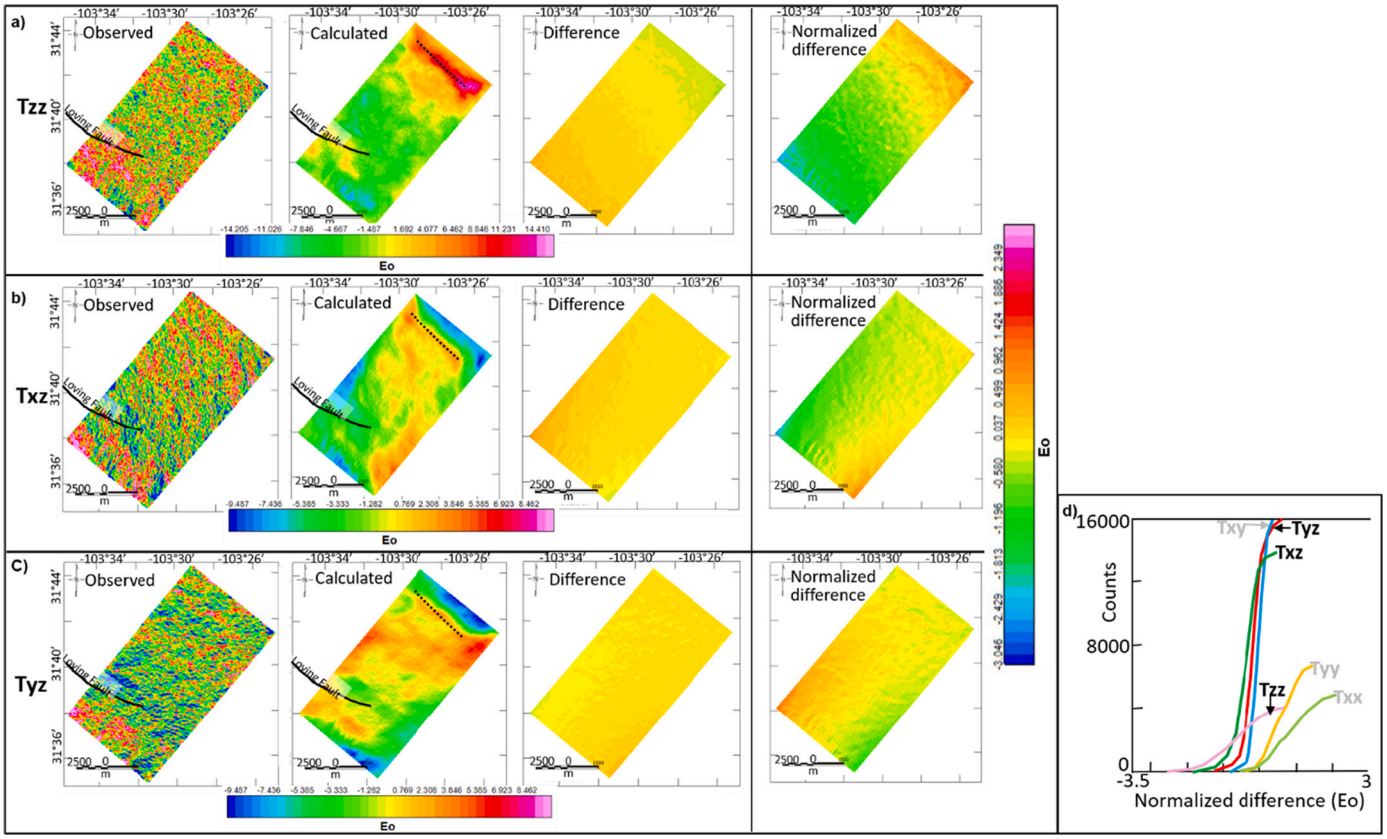

Fig. 7. Calculated components with vertical elements after Tzz density inversion of the Combined layer and normalized difference grids: a) Tzz. b) Txz. c) Tyz. The black line traces the Loving Fault. The dotted line traces the possible location of an unmapped fault. d) Normalized difference distribution of the six gravity components with vertical elements after (Tzz) density inversion of the Combined layer.

unmapped regional fault system (Fig. 5b).

The best results were achieved with the density inversion of the Combined layer (converged after 126 iterations), between topography and the top Leonardian formation, with a difference range of only −0.09 to 0.01mGal (Fig. 5c). The fit between calculated and observed gravity was further improved, indicated by a less variable normalized difference (Fig. 5c, d). Compared to the Rustler layer, the calculated gravity reveals more details in the central part of study area, a subtle correlation with the Loving Fault, and a sharper bounding gradient of the anomaly high to the northeast, and over a possible unmapped regional fault system (Fig. 5c).

3.2. *Density inversion of gravity gradient (Tzz) anomalies*

Layer densities derived from the gravity (Tz) inverse models were set as the initial densities for the gradient (Tzz) inverse models, then the same inversion workflow was employed: density inversions were conducted on the upper two layers independently, then the Combined layers. Tzz inversion converged after 257, 106, and 72 iterations for the Surface, Rustler, and Combined layer, respectively. Differences between calculated and observed Tzz were <8 Eo (or 0.008 mGal/m).

In order to better visualize each inversion result, Fig. 6 summarizes the statistical distribution of normalized differences between each observed and calculated gravity tensor after Tzz inversion. Overall, the normalized differences between observed and calculated Txy, Txz, and

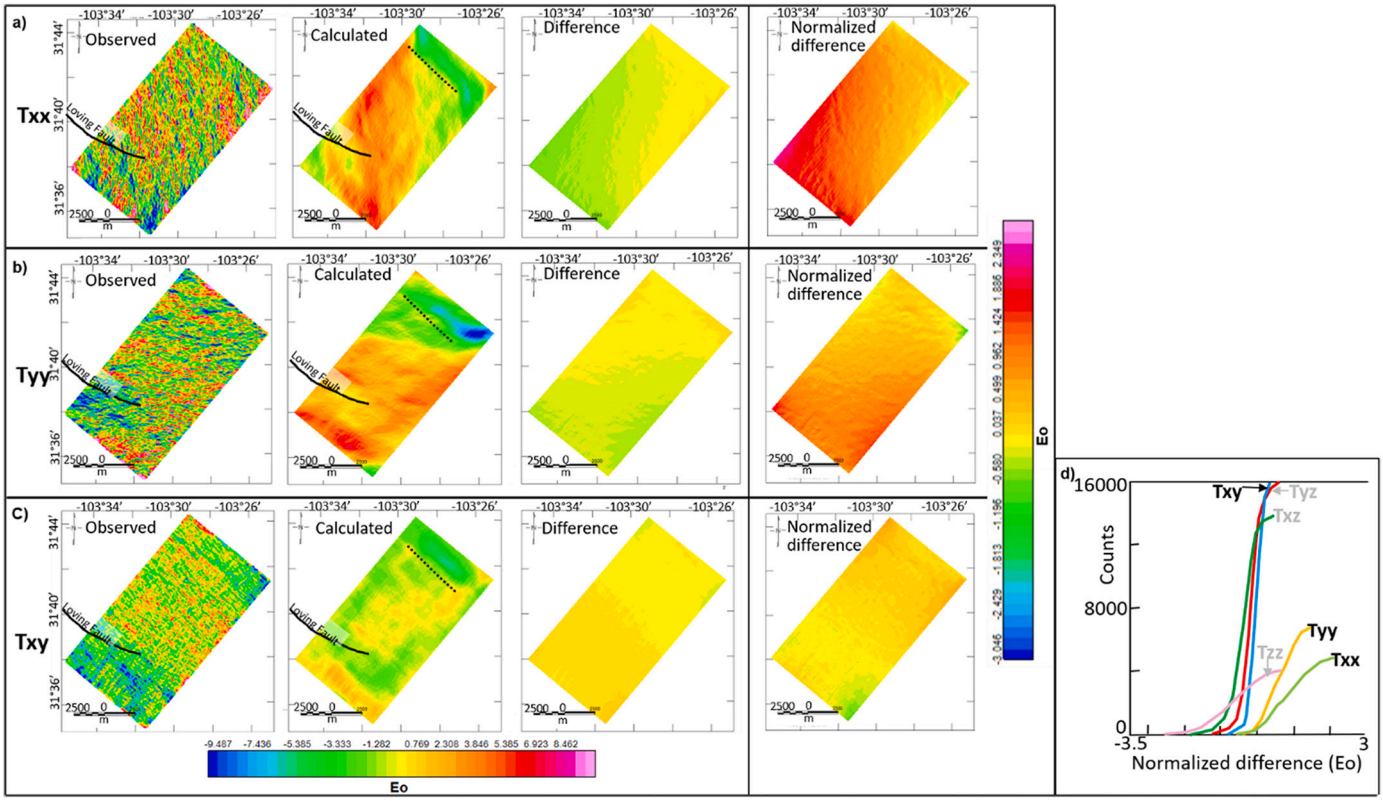

Fig. 8. Calculated components with horizontal elements after Tzz density inversion of the Combined layer and normalized difference grids: a) Txx b) Tyy. c) Txy The black line traces the Loving Fault. Note that the possible unnamed fault along the NE edge of the study area has no expression from horizontal element components. The dotted line traces the possible location of an unmapped fault. d) Normalized difference distribution of the six gravity components with horizontal elements after (Tzz) density inversion of the Combined layer.

Tyz components from all three layer inversions revealed a narrower and lower amplitude range (1.65 Eo in average) compared to the other three components (Txx, Tyy, Tzz) with a 2.98 Eo average range, indicating that the difference between these observed and calculated components are less variable and the overall modeled results are closer to the measured data. The Surface layer inversion produced a relatively broad range (2.1 to 3.8 Eo) of normalized differences for the six tensor components, suggesting, as discussed in the preceding section, that the differences between observed and calculated gravity tensors are relatively large and more variable (Fig. 6a). Normalized differences from the Rustler layer inversion, shown in Fig. 6b, also show a relatively broad range (1.6 to 4.3 Eo), indicating variable differences between the observed and calculated components, similar to Surface layer inversion, but slightly improved.

Similar to the Tz density inversion, the Combined layer inversion of Tzz produced the best result. The range of each normalized tensor component difference, especially Txy, Txz, and Tyz of the Combined layer (Fig. 6c), is narrower (<1.5 Eo); thus, less variable compared to the Surface (Fig. 6a) and Rustler layer (Fig. 6b) differences.

Fig. 7 shows the inversion results on the Combined layer of tensor components with vertical elements (Tzz, Txz, Tyz). Calculated Tzz results produce relatively high amplitude positive anomalies over the southwest and northeast parts of the model, with differences ranging from −1.21 to 3.53 Eo. The Txz component enhances N-S trending anomalies with a difference range of −7.96 to 2.72 Eo. Calculated Tyz enhances *E*-W trending anomalies, and its difference ranges from −0.76 to 1.51 Eo. The normalized differences of Txz and Tyz are less variable compared to Tzz (Fig. 7d). Thus, illustrating the relative significance of these edge detectors for interpreting gravity gradient data.

Comparisons of calculated and observed tensors with horizontal elements (Txx, Tyy, Txy) of the Combined layer are shown in Fig. 8. Calculated Txx gravity reveals subtle N-S oriented anomalies superimposed on a broader N-S trending high over the center of the study area, and its difference from the observed Txx ranges from −2.16 to 0.36 Eo. Similarly, calculated Tyy shows subtle E-W anomalies superimposed on a broader E-W trending high over the southern two-thirds of the study area. This difference ranges from −1.49 to 1.08 Eo. Calculated Txy shows a low amplitude positive anomaly over the center that broadly correlates with the observed data, having a difference that ranges from −0.61 to 1.23 Eo. The normalized difference of Txy is less variable compared to Txx and Tyy, as illustrated in Fig. 8d.

3.3. Density distributions

The density distribution generated by the Tz inversion ranges from 2.38 to 2.66 g/cc, and the Tzz density inversions produce a density range of 2.42 to 2.74 g/cc (Fig. 9). In general, these results are similar. Unsurprisingly, Tzz inverted densities display more detail than Tz. For example, all Tzz inversions of Surface, Rustler, and Combined layers produce higher densities correlating with the Loving Fault, while only the Tz inversion of the combined layers produces a slight trend over the fault (Fig. 2; Fig. 9). Rustler and Combined layer inversions produce the best Tzz density inversion results, with detailed variations in the central and southern parts of the study area, including sharp gradients that are suggestive of faults offsetting density layers or possible karst boundaries. As noted above, the NW striking density high along the northeastern edge of the area may represent an unmapped regional fault or another karst boundary.

4. Interpretation: potential karsting locations

We used Tzz inversion results of the combined layer as a guide to

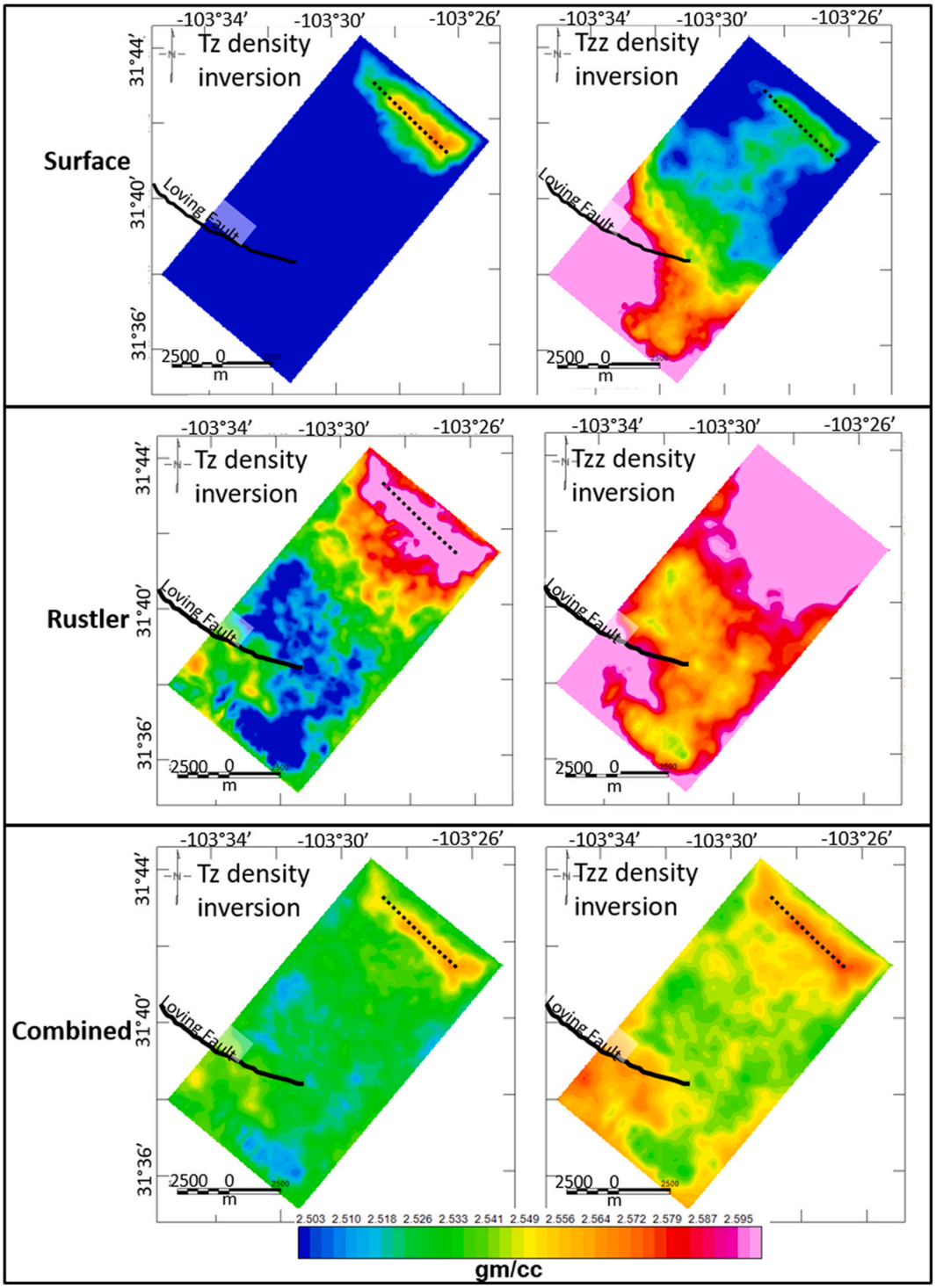

Fig. 9. Density distributions from Tz and Tzz inversions: Surface, Rustler, and Combined sedimentary layers. The NW-SW trending Loving Fault is the black line (modified from Ruppel et al., 2008). The dotted line shows the possible location of an unmapped fault.

map possible locations of hypogenic karst features. We then improved our interpretation by focusing on calculated Txz and Tyz tensor components because 1) the final inversion Tzz differences range was small (0.7–8 Eo), 2) their physical edge-defining character based on the North-East-Down (NED) standard, and 3) their inversion results are easier to map compared to the measured data (Fig. 6c). Calculated Txz anomalies from the Tzz inversion reveal source edges oriented at high angles to the west-to-east computation direction (Fig. 3b). Therefore, following the calculated anomalies from our model in Fig. 3b, we drew black lines through positive anomalies related to eastern edges of low-density source bodies, and we drew dashed black lines through negative anomalies related to western edges of low-density source bodies (Fig. 3b, Fig. 10a). Similarly, calculated Tyz anomalies reveal source edges oriented at high angles to the south-to-north computation direction.

Based on the characteristics discussed above, we drew black lines through positive anomalies related to northern edges of low-density source bodies and dashed black lines through negative anomalies related to southern edges of low-density source bodies (Fig. 3b,

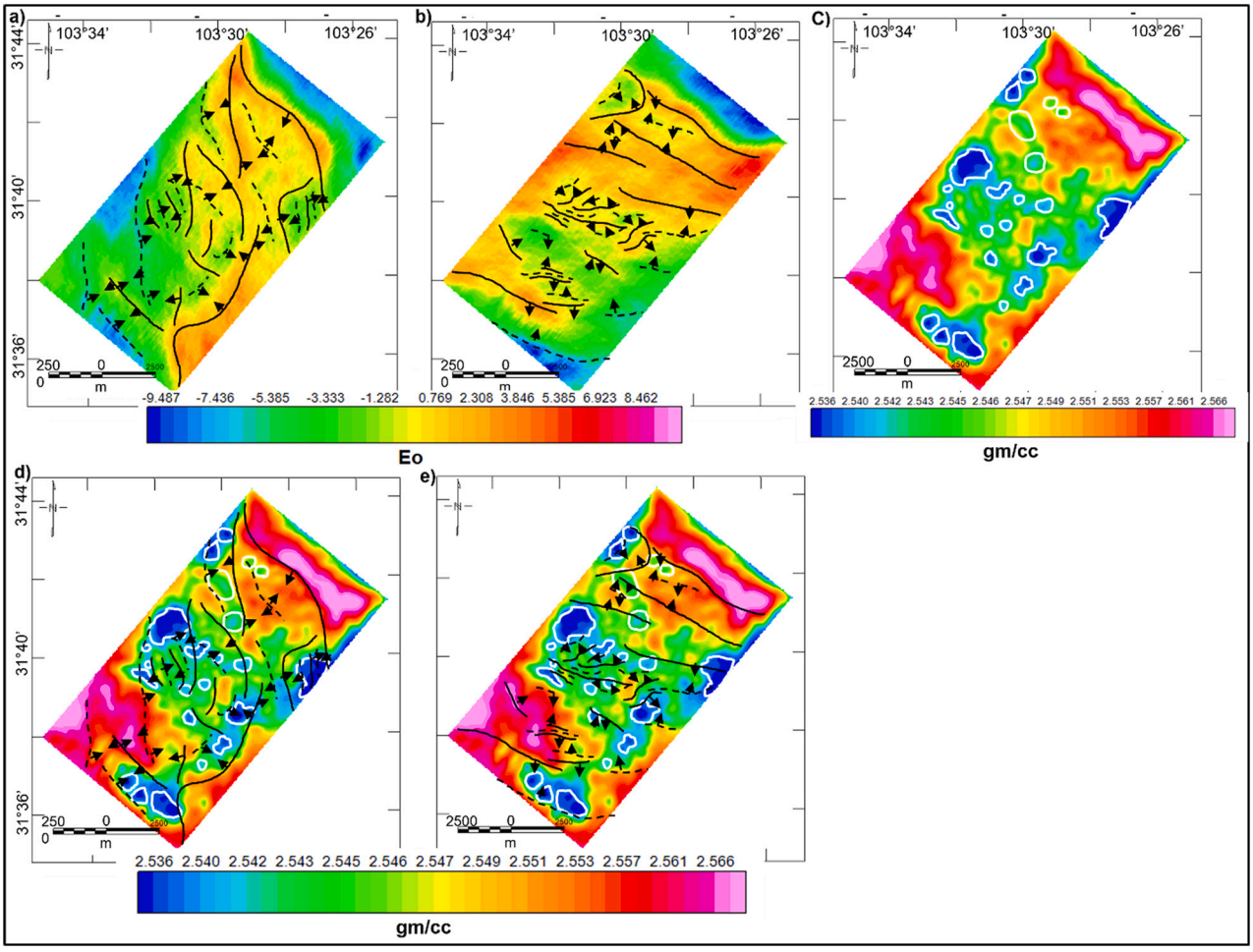

Fig. 10. a) Calculated Txz anomalies from the Tzz density inversion on the Combined layer. Black lines trace positive anomalies and suggest an eastern low-density source body edge, while dashed black lines trace negative anomalies and suggest a western low-density source body edge. Arrows point towards low-density source bodies. b) Calculated Tyz from Tzz inversion on the Combined layer. Black lines trace positive anomalies and suggest a northern low-density source body edge, while dashed black lines trace negative anomalies and suggest a southern low-density source body edge. c) Inverted densities from Tzz density inversion on the Combined layer. Lower densities are outlined in white, correlating with the edges mapped in a) and b). d) Inverted densities with low-density outlines and mapped source edges from a). d) Inverted densities with low-density outlines and mapped source edges from b).

Fig. 10b). We then combined these directional results with the Tzz density inversion to interpret probable hypogenic karst locations (Fig. 10c). The locations of low-density anomalies correlate well with the mapped source edges from the resulted Txz and Tyz (Fig. 10d, e). These may be considered higher drilling risk locations. Density inversion results of the northeastern study region show fewer low-density areas; thus, they may be considered lower drilling risk locations.

5. Discussion

Much has been studied and written about gravity gradients and the many methods for processing and interpreting these data. For example, several ideas have been tested for denoising alone, from survey design, to gridding and spectral analyses, equivalent source techniques, directional filtering, and inversion (While et al., 2006; Pajot et al., 2008; Barnes and Lumley, 2011; Yuan et al., 2013; Barnes, 2014; Brewster et al., 2014; Christensen et al., 2014; Pilkington and Shamispour, 2014; Martinez and Li, 2016; Brewster, 2017). Regarding interpretation, inversion algorithms might be the most tested ideas, including use of fixed source geometries, depth estimation, cokriging, analytic signal, downward continuation, curvature, deconvolution, radial gradients, potential field migration, and joint inversions with other geophysical data such as gravity and seismic (Zhdanov et al., 2004; Mikhailov et al., 2007; Beiki, 2010; Oruc, 2010; Zhdanov et al., 2010; Beiki and Pedersen, 2011; Zhdanov et al., 2012; Oliveira Jr. and Barbosa, 2013; Walker et al., 2013; Geng et al., 2014; Capriotti and Li, 2015; Cevallos and Kovac, 2015; Zhou, 2016; Zhou and Jiao, 2016; Lin and Zhdanov, 2017; Sun et al., 2020). Edge detection is also an aspect of interpretation that has included a great deal of work, such as filtering, directional gradients, balanced gradients, eigenvalue analyses, curvature, and worming (Murphy and Brewster, 2007; Veryaskin and McRae, 2008; Fu-Yu and Li-Kun, 2012; Cevallos et al., 2013; FitzGerald and Milligan, 2013; Zhou et al., 2013; Lu and Ma, 2015; Zou and Hu, 2015; Yuan et al., 2016).

Experienced interpreters of gravity data, as well as magnetic data, are often able to examine anomaly maps and make quick geological inferences based on anomaly wavelengths and amplitudes. That is, in their minds, they have a catalog of geological structures and lithologies that may likely produce the pattern and character of a given anomaly map. Unfortunately, applications of the methods listed above produce results that quite often do not resemble the original gradient components. In other words, extensive computation seems to always be required to interpret these data. Except for Txz and Tyz. Geologic meaning may be directly inferred by an examination of these components. One knows that Txz maxima, generally trending north-south, are located over an edge and density is increasing west to east; and that Tyz maxima, generally trending east-west, are located over an edge and

density is increasing from south to north. Perhaps direct interpretation of Txz and Tyz components may be a step towards building an interpretation catalog for gradient data.

6. Conclusions

Terrain corrected FTG data are useful for near-surface detailed studies because subtle density variations can be accurately mapped and modeled. The focused survey size and ultra-short acquisition line spacings in this study gave us an excellent opportunity to examine an area in detail for subtle density variations in the near-surface sedimentary section. By integrating surrounding geological measurements and gravity modeling, we are able to interpret regions lacking subsurface measurements due to karsting. We present a seldom used, but simple approach for interpreting the high-resolution gravity gradient data and note that this integrated workflow may be applied to other regions that contain low-density geobodies. Low-density source body edges, outlined by measured Txz and Txy anomalies, indicate locations of possible hypogenic karst features. Integrating this approach with traditional 3D inverse density modeling of Tzz data clarifies the density distribution better than Tz density inversion alone, including steep gradients that suggest large fault offsets. We conclude that the central and southwestern parts of the study area are at higher risks for drilling, while the northeastern part of the study area is at lower risk.

Declaration of Competing Interest

There is a potential conflict of interests between this study and the researches in Dr. Jiajia Sun's group at the University of Houston.

Data availability

The data that has been used is confidential.

Acknowledgements

We thank Bell Geospace for kindly providing the FTG data survey and Enverus for providing the well-log data used in this study. We thank Seequent for providing the educational license of the *Oasis montaj* software that was used for gravity modeling. We thank Scott Payton and Alan Morgan at Bell Geospace and Josh Sellars at Seequent for sharing their knowledge and insights. We thank the industry sponsors of the Conjugate Basins, Tectonics, and Hydrocarbons consortium at the University of Houston for their continuing support.

References

Adams, D.C., Keller, G.R., 1996. Precambrian basement geology of the Permian Basin region of West Texas and eastern New Mexico: a geophysical perspective. AAPG Bull. 80 (3), 410–431.
Barnes, G., 2014. Reconstructing the gravity gradient anomaly field from surveys with wide line spacing using equivalent source processing: an error analysis. Geophys. Prospect. 62, 646–657.
Barnes, G.J., Lumley, J.M., 2011. Processing gravity gradient data. Geophysics 76 (2), 133–147.
Beiki, M., 2010. Analytic signals of gravity gradient tensor and their application to estimate source location. Geophysics 75 (6), 159–174.
Beiki, M., Pedersen, L.B., 2011. Window constrained inversion of gravity gradient tensor data using dike and contact models. Geophysics 76 (6), 159–172.
Bell, R.E., Anderson, R., Pratson, L., 1997. Gravity gradiometry resurfaces. Lead. Edge 16 (1), 55–59.
Blakely, R.J., 1995. Potential Theory in Gravity and Magnetic Applications. Cambridge University Press.
Bott, M.H.P., 2012. Inverse methods in the interpretation of magnetic and gravity anomalies. In: Methods in Computational Physics, 13, pp. 133–162.
Brewster, J., 2017. Gravity gradiometer design comparison by analysis of parametric inversion. In: Society of Exploration Geophysicists, International Exposition and 87th Annual Meeting, pp. 1739–1743.
Brewster, J., Mataragio, J., Murphy, C., 2014. A self steering directional filter for focused imaging of Full Tensor Gradiometer data. In: Society of Exploration Geophysicists, International Exposition and 84th Annual Meeting, pp. 1334–1338.
Capriotti, J., Li, Y., 2015. Integrating gravity and gravity gradiometry data for joint inversion: a case study at the Kauring Test Site. In: Society of Exploration Geophysicists International Exposition and 85th Annual Meeting, pp. 1505–1509.
Cevallos, C., Kovac, P., 2015. 3D geophysical model of the Glyde Basin, Northern Territory, based on curvatures derived from airborne gravity gradient data. In: Australian Society of Exploration Geophysicists – Petroleum Exploration Society of Australia 24th International Geophysical Conference and Exhibition, pp. 1–4.
Cevallos, C., Kovac, P., Lowe, S.J., 2013. Application of curvatures to airborne gravity gradient data in oil exploration. Geophysics 78 (4). G818-G88.
Christensen, A.N., van Galder, C., Dransfield, M., 2014. Improved resolution of fixed-wing airborne gravity gradiometer surveys. In: Society of Exploration Geophysicists International Exposition and 84th Annual Meeting, pp. 1319–1323.
Cordell, L., Henderson, R.G., 1968. Iterative three-dimensional solution of gravity anomaly data using a digital computer. Geophysics 33 (4), 596–601.
Dransfield, M., Le Roux, T., Burrows, D., Lane, R.J.L., 2010. Airborne gravimetry and gravity gradiometry at Fugro Airborne Surveys. In: Airborne Gravity 2010-Abstracts, ASEG-PESA Airborne Gravity 2010 Workshop, pp. 49–57.
Dutton, S.P., Kim, E.M., Broadhead, R.F., Breton, C.L., Raatz, W.D., Ruppel, S.C., Kerans, C., 2004. Play analysis and digital portfolio of major oil reservoirs in the Permian Basin. In: Application and Transfer of Advanced Geological and Engineering Technologies for Incremental Production Opportunities, pp. 1–428. https://doi.org/10.2172/828411. https://www.osti.gov/servlets/purl/828411, accessed Jan 15, 2019.
Dutton, S.P., Kim, E.M., Broadhead, R.F., Raatz, W.D., Breton, C.L., Ruppel, S.C., Kerans, C., 2005. Play analysis and leading-edge oil-reservoir development methods in the Permian Basin: increased recovery through advanced technologies. AAPG Bull. 89 (5), 553–576.
Ennen, C., 2012. Mapping Gas-Charged Fault Blocks around the Vinton Salt Dome, Louisiana Using Gravity Gradiometry Data. Doctoral dissertation,. University of Houston.
Ewing, T.E., Barnes, M.A., Denison, R.E., 2019. Proterozoic Foundations of the Permian Basin, West Texas and Southeastern New Mexico — a review. In: Ruppel, S.C. (Ed.), 2019, Anatomy of the Paleozoic basin: the Permian Basin, USA (vol.1, ch. 3): The University of Texas at Austin, Bureau of Economic Geology Report of Investigations 285, 118. AAPG Memoir, pp. 63–96. https://doi.org/10.23867/R10285-1.
FitzGerald, D., Milligan, P.R., 2013. Defining a deep fault network for Australia, using 3D "worming". In: Australian Society of Exploration Geophysicists, Extended Abstracts, 1, pp. 1–4.
Fu-Yu, J., Li-Kun, G., 2012. Edge enhancement of gravity anomalies and gravity gradient tensors using an improved small sub-domain filtering method. Appl. Geophys. 9 (2), 119–130.
Garcia, E.S., Sandwell, D.T., Smith, W.H., 2014. Retracking CryoSat-2, Envisat and Jason-1 radar altimetry waveforms for improved gravity field recovery. Geophys. J. Int. 196, 1402–1422. https://doi.org/10.1093/gji/ggt469.
Geng, M., Huang, D., Yang, Q., Liu, Y., 2014. 3D inversion of airborne gravity-gradiometry data using cokriging. Geophysics 79 (4), G37–G47.
Hall, S.A., Bird, D.E., McLean, D.J., Towle, P.J., Grant, J.V., Danque, H.A., 2018. New constraints on the age of the opening of the South Atlantic basin. Mar. Pet. Geol. 95, 50–66.
Hoang, P., Soofi, K., Boyle, P., Lascaud, B., 2019. An Integrated Workflow to Detect and Avoid Shallow Karst Drilling Hazards in the Delaware Basin: Unconventional Resources Technology Conference, Denver, Colorado, 22-24 July 2019, pp. 4852–4872.
Li, X., Chouteau, M., 1998. Three-dimensional gravity modeling in all space. Surv. Geophys. 19 (4), 339–368.
Lin, W., Zhdanov, M.S., 2017. Joint inversion of seismic and gravity gradiometry data using Gramian constraints. In: Society of Exploration Geophysicists International Exposition and 87th Annual Meeting, pp. 1734–1738.
Lu, P., Ma, G., 2015. Balanced gradient methods for the interpretation of gravity tensor gradient data. J. Appl. Geophys. 121, 84–92.
Majzoub, A.F., Stafford, K.W., Brown, W.A., Ehrhart, J.T., 2017. Characterization and delineation of gypsum karst geohazards using 2D electrical resistivity tomography in Culberson County, Texas, USA. J. Environ. Eng. Geophys. 22 (4), 411–420.
Martinez, C., Li, Y., 2016. Denoising of gravity gradient data using an equivalent source technique. Geophysics 81 (4), G67–G79.
Martinez, C., Li, Y., Krahenbuhl, R., Braga, M.A., 2013. 3D inversion of airborne gravity gradiometry data in mineral exploration: a case study in the Quadrilátero Ferrífero, Brazil. Geophysics 78 (1), B1–B11.
Mataragio, J., Kieley, J., 2009. Application of full tensor gradient invariants in detection of intrusion-hosted sulphide mineralization: implications for deposition mechanisms. First Break 27 (7), 1–4.
Mikhailov, V., Pajot, G., Diament, M., Price, A., 2007. Tensor deconvolution: a method to locate equivalent sources from full tensor gravity data. Geophysics 72 (5), 161–169.
Morgan, R.A., Jorgensen, G., Payton, S., Stafford, K.W., 2018. Detection and Avoidance of Karst Related Shallow Geohazards Using Ultra High Resolution Full Tensor Gravity Gradiometry in the Delaware Basin, Texas. AAPG ACE Abstract.
Murphy, C.A., 2004. The Air-FTG airborne gravity gradiometer system. In: ASEG- PESA Airborne Gravity 2004 Workshop, pp. 7–14.
Murphy, C.A., Brewster, J., 2007. Target delineation using Full Tensor Gravity Gradiometry data. In: Australian Society of Exploration Geophysicists, Extended Abstracts, 1, pp. 1–3.
Murphy, C.A., Dickson, J.L., 2009. Exploring exploration play models with FTG gravity data. In: 11th SAGA Biennial Technical Meeting and Exhibition, pp. 89–91.
Murphy, C.A., Mumaw, G.R., 2004. 3D Full Tensor Gradiometry: a high resolution gravity measuring instrument resolving ambiguous geological interpretations. ASEG Extended Abstr. 2004 (1), 1–4.

Oliveira Jr., V.C., Barbosa, V.C.F., 2013. 3-D radial gravity gradient inversion. Geophys. J. Int. 195, 883–902.
Oruc, B., 2010. Depth estimation of simple causative sources from gravity gradient tensor invariants and vertical component. Pure Appl. Geophys. 167, 1259–1272.
Pajot, G., de Viron, O., Diament, M., Lequentrec-Lalanceete, M.-F., Mikhailov, V., 2008. Noise reduction through joint processing of gravity and gravity gradient data. Geophysics 73 (3), I23–I34.
Parker, R.L., 1973. The rapid calculation of potential anomalies. Geophys. J. Int. 31 (4), 447–455.
Pilkington, M., Shamispour, P., 2014. Noise reduction procedures for gravity gradiometer data. In: Society of Exploration Geophysicists International Exposition and 84th Annual Meeting, pp. 1308–1312.
Ruppel, S.C., Loucks, R., Kerans, C., Jones, R.H., Nance, H.S., Breton, C.L., Hamlin, S., Gale, J., Kane, J., McDonnell, A., Guevara, E., Wang, F., Reed, R., Wright, W., Rowe, H., Guven, N., Day-Stirrat, R., Jarvie, D., Zeng, H., Fu, Q., 2008. Permian Basin Synthesis Project: Data and Models for Recovering Existing and Undiscovered Oil Resources from the Largest Oil-Bearing Basin in the US GIS Dataset. http://www.beg.utexas.edu/research/areas/permian-basin-synthesis.
Sallee, A., Dick, H., Sudhakar, V., Morgan, A., Payton, S., Paddock, D., 2019. Managing Drilling Losses in the Permian Using Airborne Gravity Full Tensor Gradiometry: SPE/IADC International Drilling Conference and Exhibition. OnePetro.
Scholle, P.A., Goldstein, R.H., Ulmer-Scholle, D.S., 2004. Classic Upper Paleozoic Reefs and Bioherms of West Texas and New Mexico. New Mexico Institute of Mining and Technology, Socorro, NM, pp. 1–178.
Stafford, K.W., 2013. Evaporite karst and hydrogeology of the castile formation: culberson county, texas and eddy county, New Mexico.
Stafford, K.W., 2017. Hypogene evaporite karst of the greater Delaware Basin. In: LaMoreaux, J.W. (Ed.), Hypogene Karst Regions and Caves of the World. Springer, Cham, pp. 531–542 (ch. 3),.
Stafford, K.W., Ehrhart, J.T., Majzoub, A.F., Shields, J.M., Brown, W.A., 2018. Unconfined hypogene evaporite karst: West Texas and southeastern New Mexico, USA. Int. J. Speleol. 47 (3), 1–13.
Stasinowsky, W., 2010. The advantages of the full tensor over Gz. In: Airborne Gravity 2010-Abstracts from the ASEG-PESA Airborne Gravity 2010 Workshop.
Sun, J., Melo, A.T., Kim, J.D., Wei, X., 2020. Unveiling the 3D undercover structure of a Precambrian intrusive complex by integrating airborne magnetic and gravity gradient data into 3D quasi-geology model building. Interpretation 8 (4), SS15–SS29.
Telford, W.M., Geldart, L.P., Sheriff, R., 1990. Applied Geophysics. Cambridge University Press.
Veryaskin, A., McRae, W., 2008. On combined gravity gradient components modelling for applied geophysics. J. Geophys. Eng. 5 (3), 348–356.
Walker, G., Mantovani, M., Medina, E., De Luca, L., Lovatini, A., 2013. Improving subsurface imaging with simultaneous joint inversion of land seismic and airborne gravity gradiometry data. In: Society of Exploration Geophysicists International Exposition and 83rd Annual Meeting, pp. 4780–4784.
While, J., Jackson, A., Smit, D., Biegert, E., 2006. Spectral analysis of gravity gradiometry profiles. Geophysics 71 (1), J11–J22.
Yuan, Y., Da-Nian, H., Qing-Lu, Y., Mei-Xia, G., 2013. Noise filtering of full-gravity gradient tensor data. Appl. Geophys. 10 (3), 241–250.
Yuan, Y., Gao, J.Y., Chen, L.N., 2016. Advantages of horizontal directional Theta method to detect the edges of full tensor gravity gradient data. J. Appl. Geophys. 130, 53–61.
Zhang, H., Mann, P., Bird, D.E., Rudolph, K., 2021. Integration of regional gravity modeling, subsidence analysis, and source rock maturity data to understand the tectonic and hydrocarbon evolution of the Permian Basin, West Texas. Interpretation 9 (1), 161–181.
Zhdanov, M.S., Ellis, R., Mukherjee, S., 2004. Three-dimensional regularized focusing inversion of gravity gradient tensor component data. Geophysics 69 (4), 925–937.
Zhdanov, M.S., Wilson, G.A., Liu, X., 2010. 3D imaging of subsurface structures using migration and regularized focusing inversion of gravity and gravity gradiometry data. In: Lane, R. (Ed.), Airborne Gravity 2010, Australian Society of Exploration Geophysicists – Petroleum Exploration Society of Australia Workshop: Geoscience Australia Record 2010/23 and Geological Survey of New South Wales GS2010/0457, pp. 194–203.
Zhdanov, M.S., Gribenko, A., Wilson, G., 2012. Generalized joint inversion of multimodal geophysical data using Gramian constraints. Geophys. Res. Lett. 39, L09301.
Zhou, W., 2016. Depth estimation method based on the ratio of gravity and full tensor gradient invariant. Pure Appl. Geophys. 173, 199–508.
Zhou, S., Jiao, J., 2016. A new source parameters estimation method of airborne gravity gradient tensor data. In: Australian Society of Exploration Geophysicists, Extended Abstracts, 1, pp. 1–4.
Zhou, W., Du, X., Li, J., 2013. The limitation of curvature gravity gradient tensor for edge detection and a method for overcoming it. J. Appl. Geophys. 98, 237–242.
Zou, B., Hu, 2015. Edge detection of gravity field using eigenvalue analysis of gravity gradient tensor. J. Appl. Geophys. 114, 263–270.